Acta Materialia 246 (2023) 118693

Contents lists available at ScienceDirect

Acta Materialia

journal homepage: www.elsevier.com/locate/actamat

Phase field modeling of shearing processes of a dual-lobed $\gamma''|\gamma'|\gamma''$ coprecipitate

Longsheng Feng [a,d], Rongpei Shi [b], Christopher H. Zenk [c], Michael J. Mills [a], Yunzhi Wang [a,*]

[a] Department of Materials Science and Engineering, The Ohio State University, Columbus, OH 43210, USA
[b] School of Materials Science and Engineering, Harbin Institute of Technology, Shenzhen 518055, China
[c] Department of Materials Science and Engineering, Friedrich-Alexander-Universität Erlangen-Nürnberg, Martensstr. 5, Erlangen 91058, Germany
[d] Materials Science Division, Lawrence Livermore National Laboratory, Livermore, CA 94550, USA

ARTICLE INFO

Keywords:
Precipitation hardening
Dislocation-shearing ordered precipitates
Microtwinning
Superalloys
IN718

ABSTRACT

The Ni-based superalloy IN718 is one of the most widely used commercial alloy in the aerospace industry since its development in 1960s. The excellent mechanical properties have been attributed in a great deal to strengthening by coherent γ' and γ'' precipitates. The deformation mechanisms of these two phases have been well studied individually. Recent experimental characterization has shown coprecipitates of these two phases in a variety of morphologies and it was argued that these coprecipitates may lead to improved strengthening as compared to their monolithic counterparts. However, the deformation mechanisms of these coprecipitates are still not well understood. In this study, we performed microscopic phase field simulations, with generalized-stacking-fault (GSF) energy surfaces from *ab initio* calculations as inputs, to systematically study the shearing processes of a periodical array of dual-lobed coprecipitates as well as monolithic precipitates. We found that the coupling between the γ' and γ'' phases in the coprecipitates forces dislocations to take high energy shearing pathways in both phases that would not occur if they were in monolithic forms. The coupling also creates stacking fault configurations in the coprecipitates that require high stress to form. Thus, the presence of coprecipitates in general should increase the resistance to dislocation shearing and lead to higher strength levels. Various fault configurations observed during the shearing process are documented as a reference for future comparison with experimental observations. The link between stacking fault shearing and microtwinning is also discussed. The mechanisms analyzed in this study deepens our understanding of coprecipitation effects on alloy strength and may form a cornerstone for multi-precipitate strengthened alloy design strategies.

1. Introduction

Alloy 718 and its variants show extraordinary mechanical properties at elevated temperatures and are thus widely used in aerospace as well as land-based turbines [1]. The primary strengthening precipitates in the alloy are the coherent γ' (cubic, $L1_2$, chemical prototype Ni_3Al) and γ'' (tetragonal, $D0_{22}$, chemical prototype Ni_3Nb) phases, and depending on alloy composition and heat treatment, a rich variety of precipitate microstructures have been identified in experiments [2–7]. Numerous efforts have been made to understand the processing-microstructure-property relationship to further advance the application potential of this important class of superalloys [8–14]. For instance, it was proposed that alloys containing coprecipitates, e.g., dual-lobed (or "hamburger") $\gamma''|\gamma'|\gamma''$ coprecipitates and compact coprecipitates (where all six {100} facets of cuboidal γ' precipitates are covered by γ'' phase) can improve the coarsening resistance and mechanical properties of the alloy as compared to the ones with monolithic precipitate microstructures [2,3]. Different strategies of alloy design and thermo-processing have therefore been studied to obtain a variety of these coprecipitate microstructures. Multi-phase field simulations are used to understand the nucleation mechanisms [15] and growth kinetics [16] of dual-lobed and compact coprecipitates to guide alloy design.

The deformation mechanisms of the individual γ' and γ'' phases have been investigated both experimentally [17–20] and computationally [21–25]. A deformation map for polycrystalline γ'-strengthened Ni-based superalloys was recently developed to account for the temperature dependence of creep deformation mechanisms of the γ' phase, where anti-phase-boundary (APB) shearing is active at high temperature

* Corresponding author.
E-mail address: wang.363@osu.edu (Y. Wang).

https://doi.org/10.1016/j.actamat.2023.118693
Received 27 August 2022; Received in revised form 23 December 2022; Accepted 7 January 2023
Available online 14 January 2023

regime (>750°C) whereas stacking fault shearing and microtwinning are active at intermediate temperature regime (650°C~750°C) [17]. For the γ″ phase, stacking fault was observed at room temperature with small amounts of deformation while microtwins were observed with large amounts of deformation [26]. Microscopic phase field simulations were conducted to study the shearing mechanisms of monolithic γ″ precipitates and various complicated stacking fault configurations were identified, including APB, superlattice-intrinsic-stacking-fault (SISF), APB-like fault, complex-stacking-fault (CSF), and intrinsic-stacking-fault (ISF) [24]. To understand experimental observations of some interesting fault structures observed in a dual-lobed coprecipitate [6], where HAADF STEM imaging was used to analyze the atomic structure of the fault configurations, limited microscopic phase field simulations were carried out [27] to show the detailed shearing processes. The simulation results were able to explain the experiment observations. Motivated by this success, in this study we carry out systematic microscopic phase field simulations to investigate the detailed shearing processes of an periodic array of dual-lobed γ″|γ′|γ″ coprecipitates, examine the coupling effects among dislocation shearing events in the two phases, and predict all possible fault configurations that could be observed in a dual-lobed coprecipitate in experiments. The characteristics of the associated deformation pathways are described to better inform the shearing processes of the coprecipitates. Also discussed are the effects of misfit stress, particle size and loading conditions on the shearing mechanisms. The link between stacking fault shearing and microtwinning is discussed at the end. The findings of this work may shed light on how the interplay between two coherent precipitate phases having different crystal structures in co-precipitate configurations may result in enhanced tensile and creep strength, which may open a new window in alloy design for exploiting co-precipitation of multiple phases to improve performances.

2. Methodology

The microscopic phase field (MPF) model [28,29] describes dislocation loops as thin martensitic plates with a set of non-conserved order parameters $\eta_p(\mathbf{r})$ for slip system p and spatial location $\boldsymbol{r}$. The displacement field $\mathbf{u}(\mathbf{r})$ within the slip plane associated with a dislocation can be described as $\mathbf{u}(\mathbf{r}) = \sum_p \eta_p(r)\mathbf{b}_p$, where $\mathbf{b}_p$ is the base vector corresponding to p-th slip system. For FCC crystals, since the slip system is $\langle 110\rangle\{111\}$, the base vectors are chosen to be $\mathbf{b}_1 = [10\bar{1}]/2$, $\mathbf{b}_2 = [\bar{1}10]/2$, $\mathbf{b}_3 = [0\bar{1}1]/2$. The total energy of the system is then formulated with respect to the order parameter $\eta_p(\boldsymbol{r})$ and is composed of three parts (Eq. (1)): crystalline energy E^{cryst}, gradient energy E^{grad} and elastic energy E^{el} [30].

$$F = E^{cryst} + E^{grad} + E^{el} \tag{1}$$

The crystalline energy is the generalized-stacking-fault (GSF) energy surface obtained from *ab initio* calculations, which accounts for the energy contribution arisen from the local displacement of a dislocation. It reflects the crystal symmetry and thus is periodic in nature. The gradient energy takes into account the spatial variation of eigenstrain associated with dislocations. The elastic energy is calculated by the Khachaturyan-Shatalov microelasticity theory [31], which considers the elastic distortion from the dislocation displacement field and the work done by applied stress. The formulations of these energy terms are shown in Eq. (2), (3) and (4) and more details can be referred to in Ref [30].

$$E^{crystal} = \int d\mathbf{r}\ \gamma(\eta_1, \eta_2, \eta_3) \tag{2}$$

$$E^{grad} = \int d\mathbf{r}\left[\frac{\beta}{2}\sum_{p,q}(\mathbf{m}\times\nabla\eta_p)\cdot(\mathbf{m}\times\nabla\eta_q)\right] \tag{3}$$

$$E^{el} = \frac{1}{2}\int\sum_{p,q}\frac{d^3k}{2\pi}B_{pq}(\mathbf{n})\eta_p(\mathbf{k})\eta_q^*(\mathbf{k}) - \sigma_{ij}^{ex}\int\sum_p \varepsilon_{ij}^p\eta_p dV \tag{4}$$

$\gamma(\eta_1, \eta_2, \eta_3)$ is the GSF energy surface, $\mathbf{m}$ is the slip plane normal, β is the gradient energy coefficient. $B_{pq}(\mathbf{n}) = \begin{cases} 0, & for\ \ \mathbf{n} = 0 \\ C_{ijkl}\varepsilon_{ij}^p\varepsilon_{kl}^q - n_i\sigma_{ij}^p\Omega_{jk}(\mathbf{n})\sigma_{kl}^q n_l, & for\ \ \mathbf{n} \neq 0 \end{cases}$ for a stress-controlled boundary condition, where $\mathbf{k}$ is the reciprocal space vector and $\mathbf{n}$ is the unit vector of $\mathbf{k}$ ($\mathbf{n} = \mathbf{k}/|\mathbf{k}|$), $\sigma_{ij}^p = C_{ijkl}\varepsilon_{kl}^p$ and $\Omega_{ij}^{-1}(\mathbf{n}) = C_{ijkl}n_k n_j$. The eigenstrain of dislocation with Burgers vector $\mathbf{b}_p$ is expressed as $\varepsilon_{ij}^p = \frac{\mathbf{b}_p\otimes\mathbf{m}+\mathbf{m}\otimes\mathbf{b}_p}{2d_{111}}$, where d_{111} is the interplanar spacing of the slip plane and $\otimes$ is the dyadic product of two vectors.

The time evolution of the order parameter follows the Ginzburg-Landau (TDGL) equations [32]:

$$\frac{\partial\eta_p}{\partial\tau} = -L_p\frac{\delta F}{\delta\eta_p} \tag{5}$$

where τ is the dimensionless time, L_p is the kinetic coefficient characterizing dislocation mobility. All parameters used in this work are the same as those in Ref [27] unless specified otherwise. The GSF of Ni, Ni_3Al and Ni_3Nb are used to represent γ, γ′ and γ″ phases in multi-component alloys. Such simplification may not change the shearing pathways presented in this work, but may matter in quantitative prediction of the shearing process (like critical resolved shearing stress for each shearing pathway).

3. Results

We first evaluate the number of unique dislocation configurations to consider from the symmetry analysis of the 3 phases involved, i.e., γ($Fm\bar{3}m$), γ′($Pm\bar{3}m$) and γ″($I4/mmm$). Since γ″ has the lowest point symmetry, it has the greatest number of unique combinations of dislocation groups. For a single dislocation, there are six $a/2\langle 110\rangle$ dislocations on the $(111)_\gamma$ of γ and equivalent slip planes of γ′ and γ″ phases, all of which are equivalent in the γ and γ′ phase due to the 3-fold rotational symmetry as well as the mirror symmetry with respect to the $\langle 110\rangle_\gamma$ axis. Whereas in the γ″ phase, since the 3-fold rotational symmetry is lost, there are 3 distinctive dislocations, i.e., AB(BA), AC(BC), CB(CA), following the Thompson notation [33]. Similarly, for two $a/2\langle 110\rangle_\gamma$ dislocations, there are a total of 36 combinations, only 9 of which are unique (see Fig. S10 in Supplementary Materials), i.e., three dislocations groups of like-signed $a/2\langle 110\rangle_\gamma$ dislocations (AC+AC, AB+AB and CB+CB) and six dislocation groups of unlike-signed $a/2\langle 110\rangle_\gamma$ dislocations (AC+AB, AB+AC, AB+CB, CB+AB, AC+BC and CB+CA). The equivalent pairs are labeled with the same background color in Fig. S10 and the deformation pathways of the 9 independent ones (underlined) will be studied using phase field simulations. We also simulate two cases with three consecutive like-signed $a/2\langle 110\rangle_\gamma$ dislocations where additional features are present in comparison with the two-dislocation simulations. To study the coupling of γ′ and γ″ on the shearing process, we also perform parallel simulations with monolithic precipitates. The simulation box is 256 × 512 grids and the grid length is 0.25 nm. The applied stress is 800 MPa in the total Burgers vector direction in all simulations.

3.1. Shearing mechanisms by a single $a/2\langle 110\rangle_\gamma$ dislocation

The shearing mechanism of a dual-lobed coprecipitate by a single $a/2\langle 110\rangle_\gamma$ dislocation has been systematically studied in [27]. For completeness, here we only show the shearing process without detailed explanations:

i. An AB dislocation loops the coprecipitate.
ii. An AC dislocation shears the γ′ while the leading partial of AC shears the γ″, creating ISF and leaving the trailing partial looping the γ″ lobes.
iii. CB shears the coprecipitates and creates an APB in γ′ and an APB-like fault in γ″. Since the APB-like fault is an unstable stacking fault, a remnant Shockley partial δA is nucleated to transform the APB-like fault to an ISF configuration.

Please refer to [27] for a more detailed experimental and simulation analyses of these shearing processes. The crystalline energy of the system is plotted in Fig. 1 for the shearing process. To better visualize dislocations and the high energy planar faults, crystalline energies smaller than 40 mJ/m^2 are set to be white (thus the ISF and SISF whose energies are way below this threshold will appear as white). The same plotting scheme is used for the rest of the phase field simulation results. Note that CB is equivalent to CA in Ref [27] and its interaction with the coprecipitate results in an extended $ISF_{\gamma''}|SISF_{\gamma'}|ISF''_{\gamma}$ fault configuration, where a remnant Shockley partial δA nucleates from the γ″ phase, enters the γ′ phase and converts the APB into an SISF. This will not occur if the two precipitate phases are present in their monolithic forms (Fig. S1). This coupling effect is unique to the shearing of coprecipitates and will be discussed in more detail in Section 4.

3.2. *Shearing mechanism by two consecutive* $a/2\langle 110\rangle_\gamma$ *dislocations*

Fig. 2 shows the interaction between a group of two consecutive like-signed $a/2\langle 110\rangle_\gamma$ dislocations with the coprecipitate. Fig. 2(a) shows the ABAB dislocation shearing the coprecipitate. Since both the γ′ and γ″ phases would undergo APB shearing by the first AB and restore the unfaulted (UF) configuration by the second AB, the coprecipitate undergoes the same pathway for both phases. The final configuration is $UF_{\gamma''}|UF_{\gamma'}|UF_{\gamma''}$ and the deformation pathways in both γ′ and γ″ phases are shown on the GSFs in Fig. 6 with the white arrows.

Fig. 2(b) shows the interaction between the ACAC dislocation group and the coprecipitate. The first AC creates $ISF_{\gamma''}|APB_{\gamma'}|ISF_{\gamma''}$ in the coprecipitate (inset of Frame 1 of Fig. 2(b)), with the trailing partial Aδ of AC looping the γ″ lobes. For the γ′ phase, the second AC eliminates the APB and restores the UF configuration (inset of Frame 2), while for the γ″ phase, the second AC joins with Aδ of the first AC dislocation, transforming the ISF into an APB (inset of Frame 2). The final fault configuration is $APB_{\gamma''}|UF_{\gamma'}|APB_{\gamma''}$. The deformation pathways in both γ′ and γ″ phases on the GSFs are shown in Fig. 6 with the deep blue arrows.

Fig. 2(c) shows the interaction between the CBCB dislocation group and the coprecipitate. The first CB creates the extended $ISF_{\gamma''}|SISF_{\gamma'}|ISF_{\gamma''}$ fault configuration (Frame 3), with a remnant Shockley partial δA looping the coprecipitate (inset of Frame 2; see also Fig. 1(c) for details). The leading Cδ partial of second CB shears the SISF and ISF in γ′ and γ″, creating APB and UF configurations, respectively. When the trailing δB and the remnant Shockley partial δA shears through the γ′, they eliminate the APB and restore an UF configuration in γ′. They loop around the γ″ lobes and leave the UF configuration intact. The final fault configuration is $UF_{\gamma''}|UF_{\gamma'}|UF_{\gamma''}$ with δA+δB looping around the γ″ precipitates. The deformation pathways in both γ′ and γ″ phases on the GSFs are shown on Fig. 6 with the red arrows.

Figs. 3–5 show the interaction between the remaining six possible dislocation groups consisting of two unlike-signed $a/2\langle 110\rangle_\gamma$ dislocations and the coprecipitate. For a CBAB dislocation group (Fig. 3(a)), the CB dislocation cuts into the coprecipitate, creating an APB in the γ′ phase

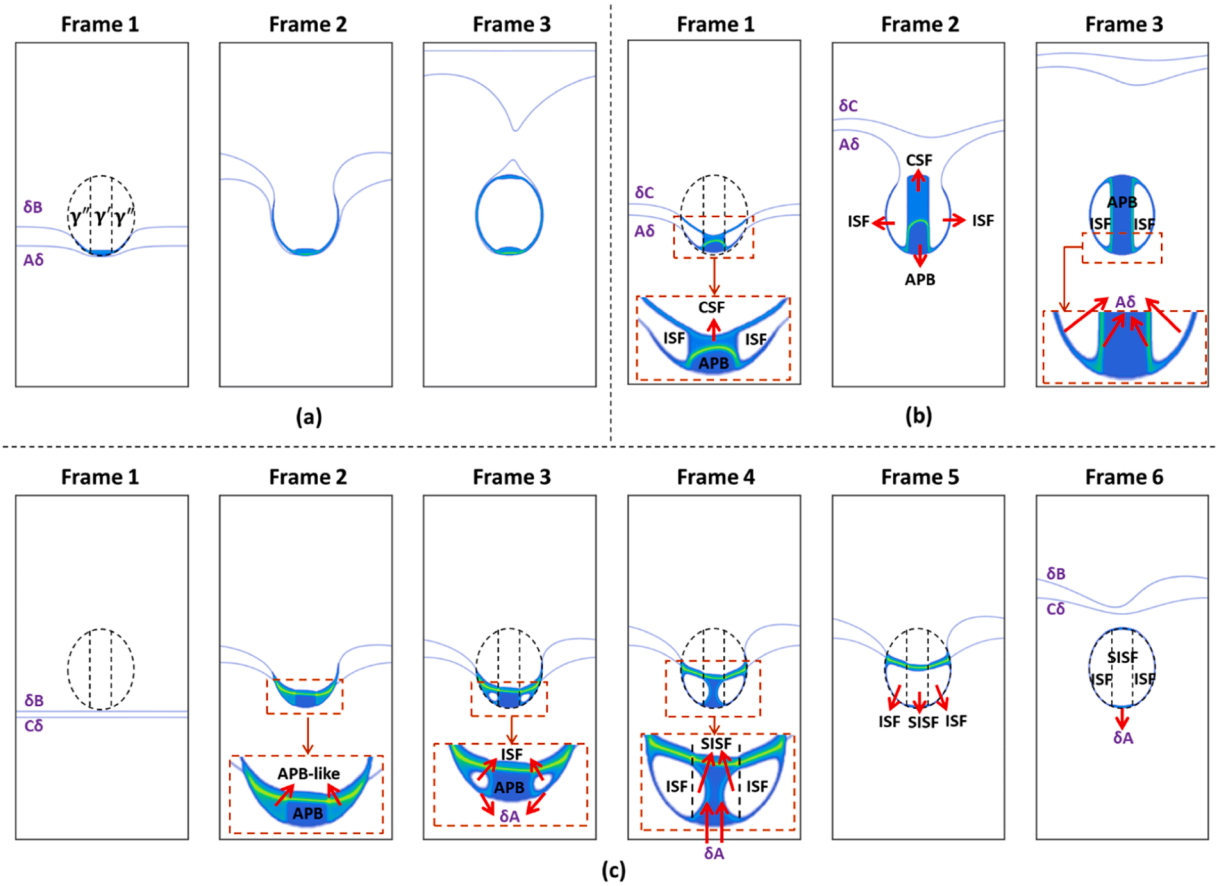

Fig. 1. Shearing of a dual-lobed coprecipitate by (a) AB, (b) AC and (c) CB dislocations. The fault is labeled by black texts and the dislocations are labeled by purple texts. The black dash line indicates the outline of the coprecipitate as well as the interface between γ′ and γ″.

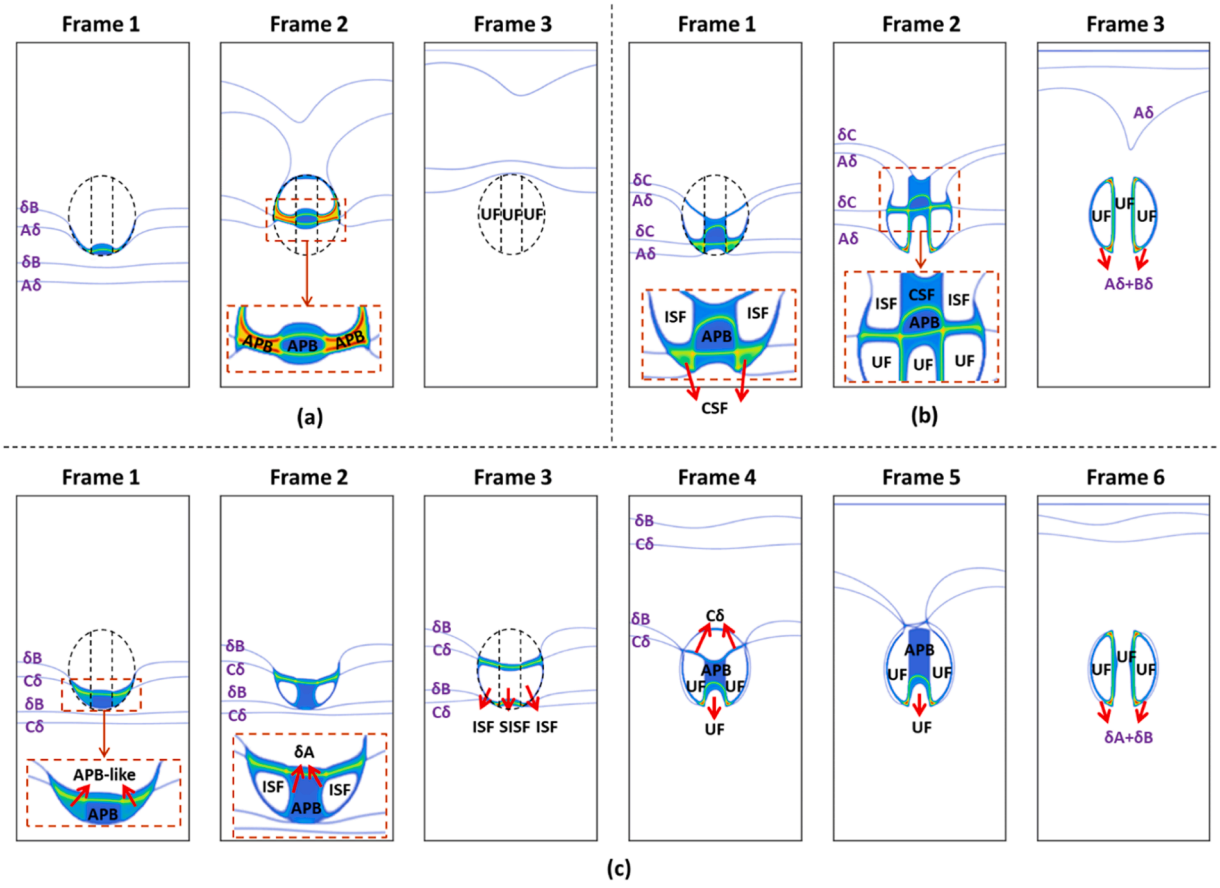

Fig. 2. Shearing of a dual-lobed coprecipitate by (a) AB+AB, (b) AC+AC and (c) CB+CB dislocation groups ($a<110>_{\gamma}$).

and APB-like faults in the γ″ phase (inset of Frame 1). Since the APB-like faults are unstable, they change spontaneously into ISFs by nucleating remnant Shockley partial δA dislocations (top inset of Frame 2). The leading partial δB of AB then cuts into the coprecipitate, creating a CSF in the γ′ phase and SISFs in the γ″ phase (bottom inset of Frame 2). The trailing partial Aδ of AB enters the coprecipitate in the end, creating an APB in the γ′ phase and APB-like faults in the γ″ phase, with the latter transforming spontaneously into ISFs by nucleating another Shockley partial δB (Frame 3). This δB partial then enters the γ′ phase and transforms the APB into an SISF (Frame 4), forming an extended $ISF_{\gamma''}|SISF_{\gamma'}|ISF_{\gamma''}$ fault configuration (Frame 5). Then the remnant Shockley partial δB loop expands into the γ matrix under the applied stress. The deformation pathways in both γ′ and γ″ phases on the GSFs are shown in Fig. 6 by the yellow arrows.

For an ABCB dislocation group (Fig. 3(b)), the AB dislocation cuts into both phases and forms an extended APB ribbon in the coprecipitate (inset of Frame 2). Just like what occurs after AB enters the coprecipitate for the CBAB dislocation group, once the CB dislocation cuts into the γ″ phase, APB-like faults are created and a remnant Shockley partial δB is nucleated to transform the APB-like faults to ISFs (Frame 3), which then enters the γ′ phase (Frame 4), transforming the APB into an SISF and further expanding into the matrix (Frame 5 and Frame 6). The final fault configuration is $ISF_{\gamma''}|SISF_{\gamma'}|ISF_{\gamma''}$ with the δB loop expanding in the matrix. The deformation pathways are shown on the GSFs in Fig. 6 by the light blue arrows. Note that both CBAB and ABCB create the same extended fault configuration after shearing, which is also the same as that after a single CB dislocation (or a single CA in Ref [27]) shearing through. The difference is that the remnant Shockley partial cannot expand in the case of single CB shearing because the applied stress is along the total Burgers vector of the initial dislocation (i.e., CB), which is perpendicular to the Burgers vector of the remnant Shockley partial δB, whereas for CBAB or ABCB, even though the applied stress is also along the total Burgers vector of the initial dislocations, it is not perpendicular to the direction of δB and thus favors the expansion of the remnant Shockley partial into the matrix. This is another scenario of getting an extended fault structure into the matrix, in addition to changing the applied stress to specifically favor the expansion of the remnant Shockley partials, as was suggested by Ref [27]. Moreover, the two pathways cannot be distinguished experimentally via atomic resolution transmission electron microscopy, because the displacement created by an AB dislocation is parallel to the atomically flat $\gamma'|\gamma''$ interface, the displacement of which is otherwise used as a tracer for the shear events [27]. Thus, the displacement analysis of this interface would give no preferential result among CB, CBAB and ABCB.

The interaction between an ACAB dislocation group with the coprecipitate has been discussed in detail in Ref [27]. Here, we only show it for completeness (Fig. 4(a)). The ABAC group (Fig. 4(b)) is equivalent to the ACAB group in both phases because in the γ′ phase, the 3-fold symmetry guarantees the equivalence, while in the γ″ phase, Lv et al [24] have showed that ABAC also follows the same shearing pathway as that of ACAB because the creation of an APB (~592 mJ/m^2) by an AB dislocation is energetically unfavorable as compared to an ISF (~2 mJ/m^2) created by the leading partial of AC. Since both dislocation groups have identical shearing pathways for both phases individually, no difference in the deformation pathway for the coprecipitate would be anticipated. As expected, the final fault configuration is $ISF_{\gamma''}|APB_{\gamma'}|ISF_{\gamma''}$ with a remnant Shockley partial δB looping the γ″ precipitates. The deformation pathways are shown on the GSFs in Fig. 6 by the orange and grey arrows.

The last two dislocation groups are CBCA and ACBC, whose interactions with the coprecipitate are shown in Fig. 5. For the CBCA dislocation group, the first three partials shear through the coprecipitate

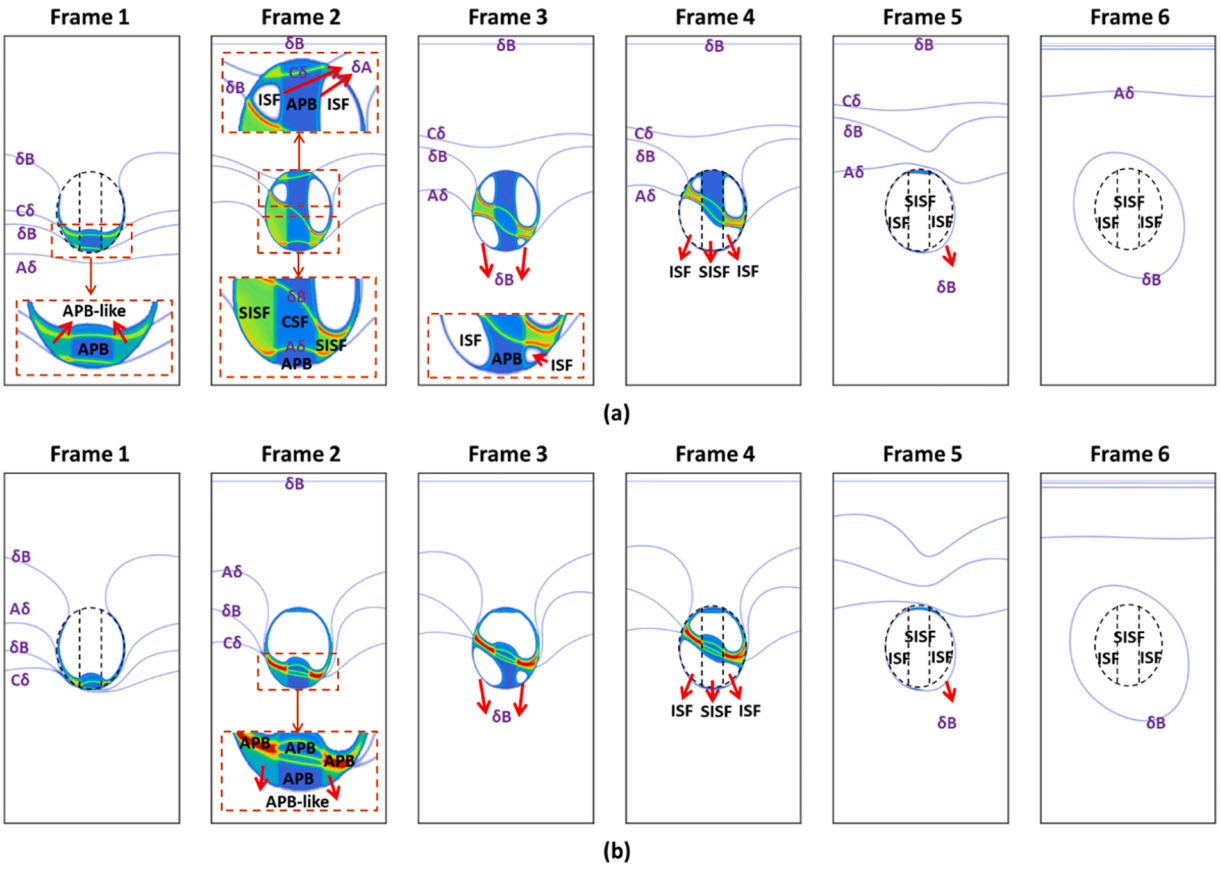

Fig. 3. Shearing of a dual-lobed coprecipitate by (a) CB+AB and (b) AB+CB dislocation groups.

as a compact dislocation and create a temporary extended $ISF_{\gamma''}|SISF_{\gamma'}|ISF_{\gamma''}$ configuration (Frame 3), which is then converted to $UF_{\gamma''}|APB_{\gamma'}|UF_{\gamma''}$ after the last partial enter the coprecipitate (Frame 4). For the ACBC dislocation group, it is the other way around so that the first partial cut into the coprecipitate and create a temporary extended $ISF_{\gamma''}|CSF_{\gamma'}|ISF_{\gamma''}$ configuration (inset of Frame 3), which is then converted to $UF_{\gamma''}|APB_{\gamma'}|UF_{\gamma''}$ after the last three partials enter the coprecipitate (Frame 4). The final fault configuration in both cases is $UF_{\gamma''}|APB_{\gamma'}|UF_{\gamma''}$ with no residual dislocation content. The deformation pathways on the GSFs are shown in Fig. 6 by the green and purple arrows.

3.3. *Shearing mechanisms of groups of more than two* $a/2\langle 110\rangle_{\gamma}$ *dislocations*

The reactions involved in shearing by dislocation combinations consisting of more than two $a/2\langle 110\rangle_{\gamma}$ dislocations are much more complicated. But most features could be expected based on the single- and two-dislocation simulations, Here, we just show two examples with unique characteristics that are not captured by the previous simulations.

Fig. 7 shows the interaction between three consecutive AC dislocations with the coprecipitate. Clearly, the third AC is not strongly coupled with the first two (Frame 2 and 3). After the first two AC dislocations shear through the coprecipitate, the fault configuration is $APB_{\gamma''}|UF_{\gamma'}|APB_{\gamma''}$ (Frame 3, see details for the AC+AC simulation in Fig. 2(c)). The third AC enters the γ' phase and creates an APB (inset of Frame 3 and Frame 4). When it enters the γ'' precipitates, it first creates SISF ribbons and APB-like faults, and then the APB-like faults transform spontaneously into ISFs bounded by remnant Shockley partials δB, which then enter the γ' precipitate and transforms the APB into an SISF. The final fault configuration is $ISF_{\gamma''}|SISF_{\gamma'}|ISF_{\gamma''}$ with a remnant Shockley partial δB looping the coprecipitate (Frame 6). This is the same configuration (both the fault and the remnant Shockley partial) as that shown in Frame 6 of Fig. 1(c), where a CB dislocation shears through the coprecipitate. As summarized in Table 1 of Section 4.1 where all final fault configurations are listed, it is rare that a specific fault configuration can only be created by one specific dislocation group/combination, which makes it experimentally challenging to determine the shearing pathway with certainty in *post-mortem* characterization. In this case, however, three instead of one dislocation shear the $\gamma'|\gamma''$ interface. This displacement can be detected in the experiment and the two shearing pathways can be discriminated even though the final fault configuration is identical [27]. The deformation pathway on the GSFs is shown in Fig. 9 by the blue arrows.

Fig. 8 shows the interaction between a CB+CB+CB dislocation group and the coprecipitate. The third CB is – as in the previous section – decoupled from the first two. The fault configuration after the first two CB dislocations have sheared through is $UF_{\gamma''}|UF_{\gamma'}|UF_{\gamma''}$ with Aδ+Bδ Shockley partials looping around the γ'' precipitates (Frame 6 in Fig. 2 (c), Frame 6 in Fig. 8). The third CB then enters the γ' phase and creates an APB (inset of Frame 8). For the γ'' phase, the third CB together with the looping Aδ+Bδ partials create an APB followed by an APB-like configuration in each of the γ'' lobes, eventually forming an ISF in each of the precipitate with a remnant Shockley partial δB looping the γ'' precipitates (Frame 9). Consequently, after the formation of the $ISF_{\gamma''}|APB_{\gamma'}|ISF_{\gamma''}$ configuration in Frame 9, with the help of applied stress, the two dislocation segments at the $\gamma'|\gamma''$ interface enter the γ' phase, eliminate the APB and leave behind a CSF in γ' while annihilating each other. The final fault configuration is $ISF_{\gamma''}|CSF_{\gamma'}|ISF_{\gamma''}$, with the remnant Shockley partial δB expanding in the matrix. This is yet another scenario where an extended fault configuration is observed in the

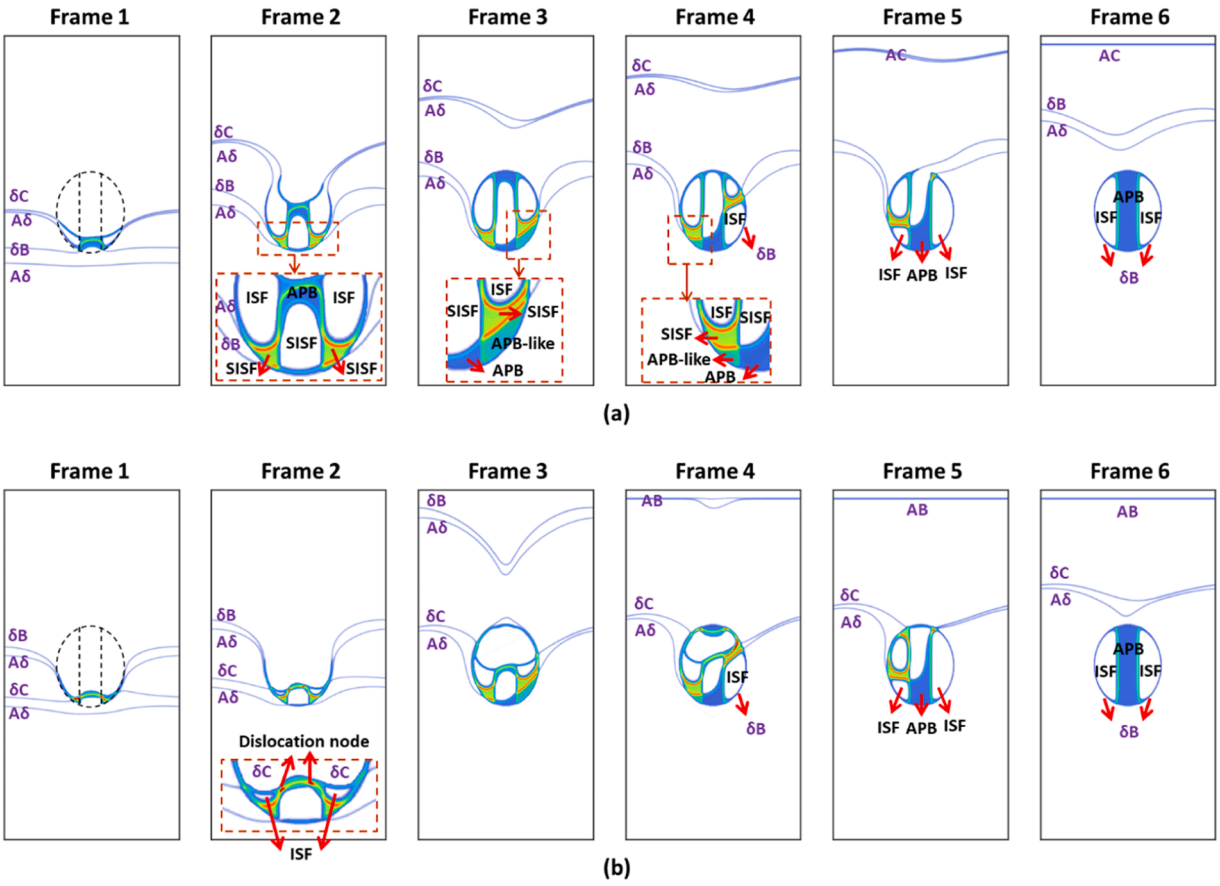

Fig. 4. Shearing of a dual-lobed coprecipitate by (a) AC+AB and (b) AB+AC dislocation groups.

coprecipitate, in addition to the CB/CA and CBAB/ABCB dislocation groups. But unlike the other four where the final configuration is $ISF_{\gamma''}|SISF_{\gamma'}|ISF_{\gamma''}$, a high energy CSF is formed in the γ' phase. This is due both to the help of the applied stress and to the unique geometry of the coprecipitate. More discussion is presented in Section 4.2. The deformation pathway on the GSFs are shown in Fig. 9 by the red arrows.

4. Discussion

4.1. Possible fault configurations in a dual-lobed coprecipitate

Even though the shearing pathways of the coprecipitate are quite complicated, the fault configurations in the coprecipitate are rather simple. Since the fault configurations observed in experiments are most likely the final configurations in the coprecipitate after the dislocations have passed through, here we summarize these final fault configurations based on our simulations results, which may serve as a reference for comparison with future experimental results. The shearing pathways associated with these fault configurations will also be discussed.

Typically, the final configuration in the precipitate can be determined directly from the one-to-one correspondence between the Burgers vector and the stacking fault. If the precipitate is sheared, the fault created in the precipitate can be directly read from the GSF energy surface. For instance, a group of $a/2\langle 110\rangle_\gamma$ dislocations always correspond to an APB or an unfaulted (UF) configuration in the γ' phase, thus the expected fault for the γ' phase after shearing by a group of $a/2\langle 110\rangle_\gamma$ dislocations is either APB or UF. However, for the γ'' phase, the $a/2\langle 110\rangle_\gamma$ full dislocations do not always correspond to a stable positions on the GSF, which is referred to as GSF mismatch [34]. For instance, an $a/2[\bar{1}01]$ (CB) dislocation corresponds to an APB-like fault on the GSF but the final fault configuration is ISF (see details in Fig. 1(c)), because the APB-like fault is an unstable stacking fault and the ISF is the nearest local energy minimum. Following this mechanism, and based on all the simulation results, we list all the possible combinations of final fault configurations in the coprecipitate, depending on what the fault directly corresponds to from the total Burgers vector for individual phases (UF or APB in γ' and UF, APB or APB-like in γ''). Table 1 shows the final fault configurations after the corresponding dislocation groups have sheared through.

Among all the possible fault configurations that groups of full dislocations could create, the UF configuration will always be the lowest energy state and should be expected the most in both phases. For an APB, because its energy in γ' is relatively low but rather high in γ'', an APB is easier to form in γ' but much harder in γ''. Consequently, if the total Burgers vector of a dislocation group creates UF in γ'', the final fault configuration in either phase will be what the total Burgers vector corresponds to on the GSF, (i.e., APB or UF in γ' and UF in γ'', first column in Table 1).

If the total Burgers vector of the dislocation group creates an APB in γ'' after it passes through, the fault configurations in γ'' can be either an APB or an UF, because the high APB energy in γ'' may lead to looping rather than shearing (second column in Table 1). This will also lead to the UF configuration in γ' despite the total Burgers vector leads to an APB in γ', because the two precipitates are connected (AB in the second column in Table 1). Note that all five of the fault configurations mentioned above cannot easily be visualized from direct high resolution STEM observations because the contrast of an APB is similar to that of UF and if the displacement is parallel to the $\gamma'|\gamma''$ interface, it is generally not detectable.

For APB-like faults, the corresponding fault in γ' can only be APB, not UF, and this is the fault configurations that have been identified in the

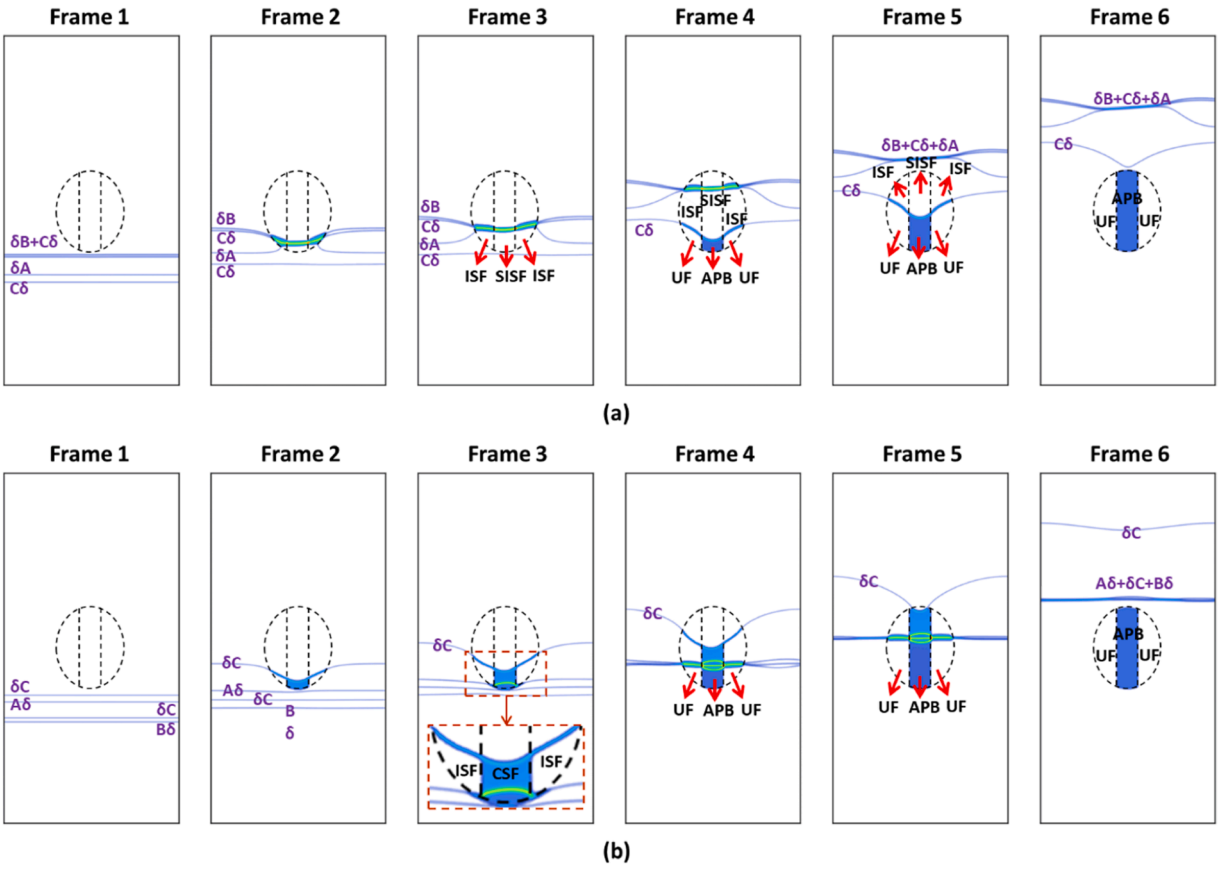

Fig. 5. Shearing of a dual-lobed coprecipitate (a) CB+CA and (b) AC+BC dislocation groups.

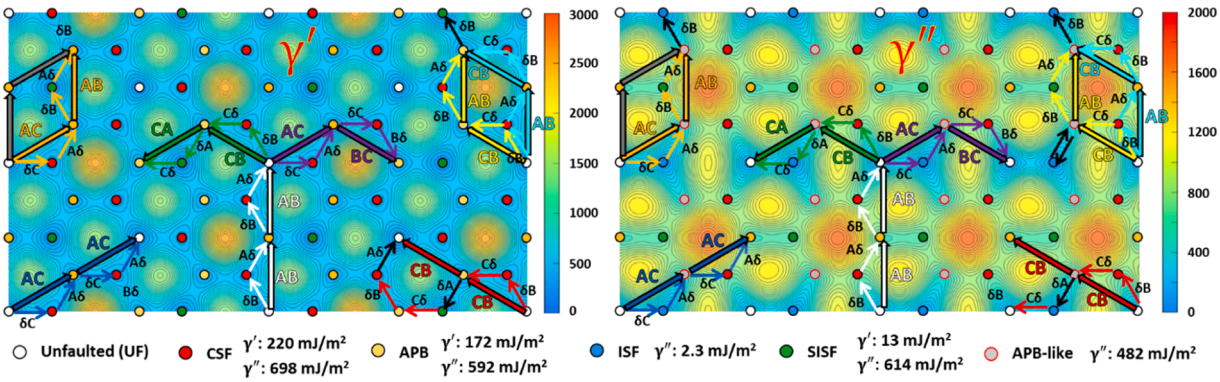

Fig. 6. Deformation pathways on the generalized stacking fault energy surfaces (GSFs) of the γ′ and γ″ phases created by different pairs of like-signed or unlike-signed $a/2\langle 110\rangle_{\gamma}$ dislocations shown in Fig. 2-5.

experiment [27]. Because the APB-like fault is unstable, it will transform into an ISF by nucleating a new Shockley partial. If that partial enters γ′, it can create either an SISF or a CSF in γ′, which are the two sub-categories in the third column. The SISF energy is usually low in γ′ and, therefore, the remnant partial can easily enter γ′, eliminating the APB and creating an SISF (i.e., $ISF_{\gamma''}|SISF_{\gamma'}|ISF_{\gamma''}$). Yet, a CSF usually has high energy in γ′ and is thus difficult to create. The remnant Shockley partial in this case can just loop the γ″ lobes, which leaves an APB in the γ′ phase (i.e., $ISF_{\gamma''}|APB_{\gamma'}|ISF_{\gamma''}$). When the applied resolved shear stress on the remnant partial is high and the elastic interaction between two parallel dislocation segments is strong (see Frame 10 in Fig. 8), such that an CSF can be formed in the γ′ phase, the remnant Shockley partial will enter γ′ and eliminate the APB by transforming it into a CSF and finally looping the entire coprecipitate (i.e., $ISF_{\gamma''}|CSF_{\gamma'}|ISF_{\gamma''}$).

Zenk et al. [27] found an atomically flat interface between γ′ and γ″ that can be used to characterize deformation of the coprecipitate, where offset of such flat interface will appear after shearing events. Based on this finding, they identified two fault configurations in Table 1, i.e., $ISF_{\gamma''}|SISF_{\gamma'}|ISF_{\gamma''}$ and $ISF_{\gamma''}|APB_{\gamma'}|ISF_{\gamma''}$. The rest of the fault configurations remain to be found in the experiment.

4.2. *Coupling effect between dislocation activities in γ′ and γ″*

To investigate synergetic – or potentially antagonistic – effects of the coupling between the γ′ and γ″ precipitates on the dislocation activities, we also performed phase field simulations with monolithic precipitates.

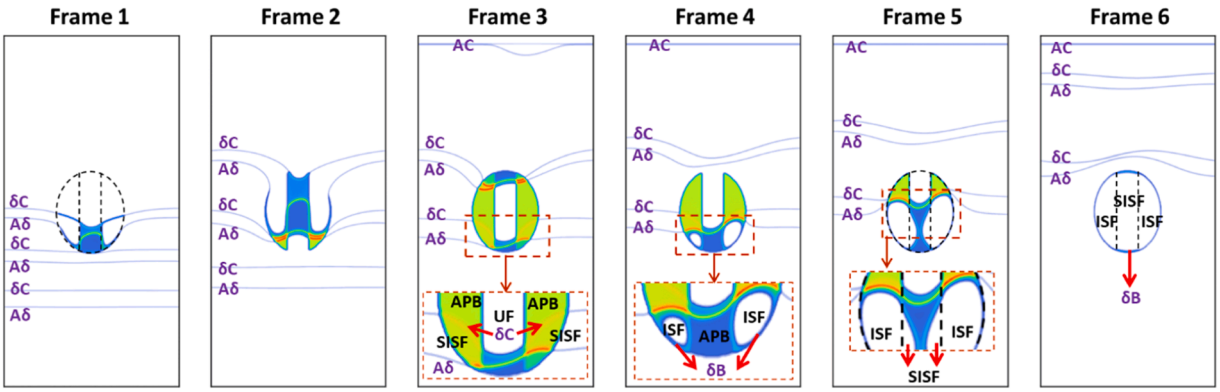

Fig. 7. Shearing of a dual-lobed coprecipitate by an AC+AC+AC dislocation group.

Table 1
Possible fault configurations in a dual-lobed coprecipitate created by different full dislocation groups.

γ″ / γ′	Unfaulted (UF)	APB	APB-like	
UF	$UF_{\gamma''}\|UF_{\gamma'}\|UF_{\gamma''}$ (ABAB)	$UF_{\gamma''}\|UF_{\gamma'}\|UF_{\gamma''}$ (CBCB) $APB_{\gamma''}\|UF_{\gamma'}\|APB_{\gamma''}$ (ACAC)		
APB	$UF_{\gamma''}\|APB_{\gamma'}\|UF_{\gamma''}$ (ACBC, CBCA)	$UF_{\gamma''}\|UF_{\gamma'}\|UF_{\gamma''}$ (AB)	$ISF_{\gamma''}\|SISF_{\gamma'}\|ISF_{\gamma''}$ (CA, ACACAC, ABCB, CBAB)	$ISF_{\gamma''}\|APB_{\gamma'}\|ISF_{\gamma''}$ (AC,ACAB, ABAC) $ISF_{\gamma''}\|CSF_{\gamma'}\|ISF_{\gamma''}$ (CBCBCB)

The shearing mechanisms of monolithic γ′ and γ″ precipitates have been widely studied experimentally and computationally. The comprehensive simulation results and deformation pathways for monolithic precipitates are included in the Supplementary Materials. The area fraction of each monolithic precipitate phase is set to be the same as that in the coprecipitates. The monolithic γ′ particle has a cuboidal shape with a triangular or hexagonal {111} cross section. The triangular cross section is used without losing any generality on the shearing pathways. The monolithic γ″ particle has a squicular [27] with an ellipse {111} cross section. By comparing the shearing processes of the coprecipitate (Section 3.1-3.3) with those of the monolithic precipitates (See Supplementary Material for detailed simulations), we identify the coupling effects between dislocation activities in the two adjacent phases due to the geometry of the dual-lobed precipitate in the following three aspects.

First, because of the coupling, dislocation shearing in each phase is forced take a high energy pathway that would not be possible if the precipitate is present in the monolithic form. A clear example is the CB+CB dislocation group shearing, where for the coprecipitate, the γ′ phase undergoes a deformation pathway of UF→CSF→APB→SISF→APB→CSF→UF (upper pathway in Fig. 10(a)), while for the monolithic precipitates, the deformation pathway for the γ″ phase is UF→CSF→APB→CSF→UF (lower pathway in Fig. 10(a)). An additional APB+SISF is present for the γ′ phase in the coprecipitate because of the remnant Shockley partial created in the γ″ phase, which adds additional strengthening effect. This is a clear example that the presence of γ″ can influence the γ′ deformation mechanisms. The coupling is also present the other way around, i.e., the presence of γ′ impacts on the deformation mechanisms of γ″. For example, for the CB+CB+CB dislocation group shearing of the coprecipitate: when the third CB shears the coprecipitate (Frame 7, Fig. 8), an APB is formed during the process in γ″, whereas in the monolithic particles, an SISF is formed in γ″. This is because SISF shearing is the lower energy pathway for the γ″ phase while the APB pathway is preferred by the γ′ phase. The deformation pathways of the γ″ phase in the initial shearing processes are mapped on the GSF in Fig. 10(c) and (e) with the red dots. Without the coupling effect from the γ′ phase, i.e., in the monolithic precipitates, the SISF formation is clearly preferred by the γ″ phase. Because the two phases are in contact with each other, the deformation pathways of the two phases must be closely coupled. The resulting high energy pathways should lead to a higher shear resistance by the coprecipitate than that by the monolithic counterparts.

Second, for the same deformation pathway, the fault configuration in the precipitates can be different between coprecipitate and monolithic precipitates. For instance, in the interaction between ABAB dislocation group and the two precipitate microstructures, both precipitate microstructures undergo APB ribbon shearing. For the monolithic ones, the two AB dislocations in the γ′ phase are clearly weakly coupled (Fig. 11 (b)), i.e., the two dislocations do not cut the precipitate at the same time. But for the coprecipitate, since the γ″ phase has a much higher APB energy than that of the γ′ phase, the full dislocation pair is strongly coupled—even in the γ′ phase. According to the theory of precipitation strengthening, the strength increments from weakly and strongly coupled dislocations with small precipitates can be calculated as

$$\Delta\tau_{weak} = 0.5\left(\frac{E_{APB}}{b}\right)^{1.5}\left(\frac{bdf}{\Gamma}\right)^{0.5}A - \frac{0.5E_{APB}}{b}f$$

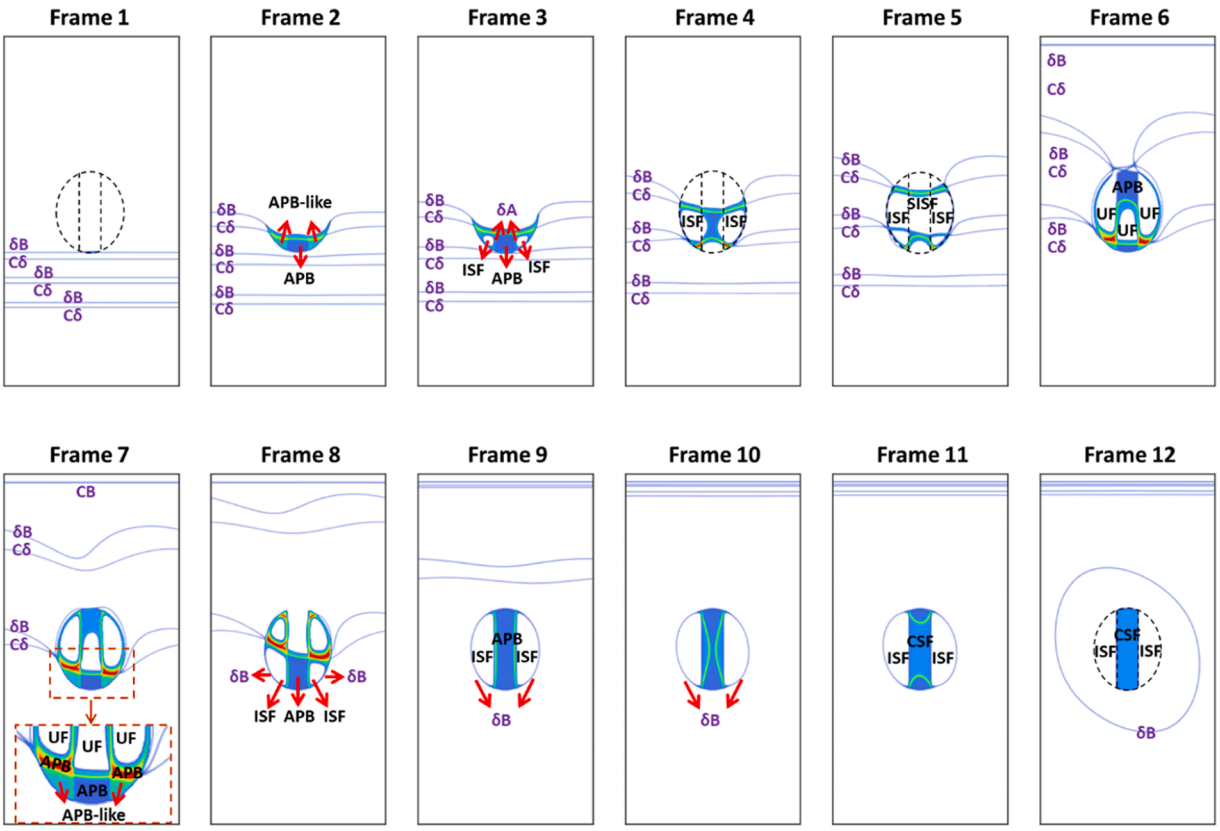

Fig. 8. Shearing of a dual-lobed coprecipitate by a CB+CB+CB dislocation group.

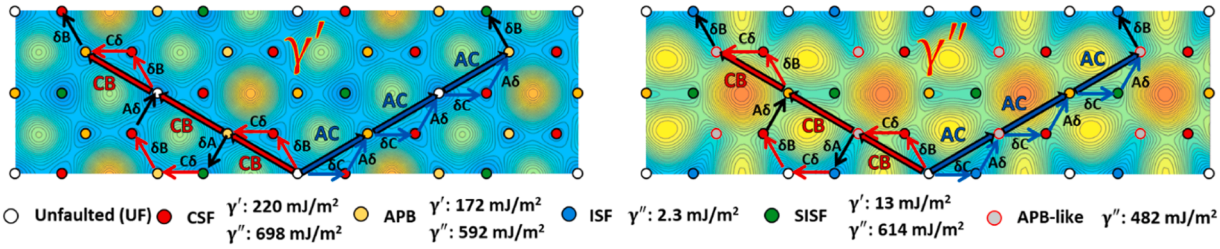

Fig. 9. Deformation pathways on the GSFs of γ′ and γ″ phases created by three consecutive like-signed AC ($a/2\langle 110\rangle_\gamma$) dislocations shown in Fig. 7 and Fig. 8.

and

$$\Delta\tau_{strong} = \frac{0.86\Gamma f^{0.5} w}{bd}\left(\frac{1.28dE_{APB}}{w\Gamma} - 1\right)^{0.5},$$

respectively, where E_{APB} is the APB energy, b is the Burgers vector, d is the diameter of a spherical precipitate, f is the volume fraction of the precipitate, Γ is the line tension of the dislocation, A is a pre-factor for precipitate shape (0.72 for spherical particles) and w characterizes the elastic interaction between two strongly-coupled full dislocations [35, 36]. For the same precipitate size, the strongly coupled dislocations give rise to a larger contribution to the strength (Fig. 12). This means that the γ′ phase in the coprecipitate has a larger shear resistance than that in the monolithic form because the dislocations cannot shear individually and are instead forced to be strongly coupled. A similar situation is observed in the case of the ACAB dislocation group shearing (Fig. 11(c) and (d)), where an SISF is created in both γ′ and γ″ phases. But because the two particles in the coprecipitate are adjacent to each other, the high energy SISF in γ″ is connected to the low energy SISF in γ′, thus a wider SISF ribbon is observed in the γ″ phase in the coprecipitate (Fig. 11(c)) as compared to that in the monolithic particles (Fig. 11(d)), which also creates larger shear resistance.

Third, there is a strong elastic interaction between dislocation loops due to the geometry of the γ″ phase in the coprecipitate. Because the γ′|γ″ interface is flat and the two lobes of γ″ are forced to be close with each other, if dislocations loop the γ″ particles, there is a strong elastic attraction between the two segments at the γ′|γ″ interface, which have the same Burgers vector but opposite line directions. This means that the segment will try to enter the γ′ phase in the middle and annihilate each other, leading to the formation of extended faults. However, often times shearing would result in a high energy configuration for γ′, such as a CSF, and thus the shearing will not proceed. Yet with high enough applied stress, this can happen. This is demonstrated by the interaction between CB+CB+CB dislocation group and the coprecipitate. The final fault configuration in the coprecipitate is $ISF_{\gamma''}|CSF_{\gamma'}|ISF_{\gamma''}$ (Fig. 13(a)). The CSF in γ′ is rarely extended due to its high energy, but it can form here because the partials that create it are driven by the applied stress, in addition to strong elastic attractions from the two parallel dislocation segments at the γ′|γ″ interface, which does not exist for monolithic precipitates. In the monolithic precipitates (Fig. 13(b)), even though the applied stress is the same as that in the case of the coprecipitate, which drives the expansion of the partial, the elastic attraction is much weaker

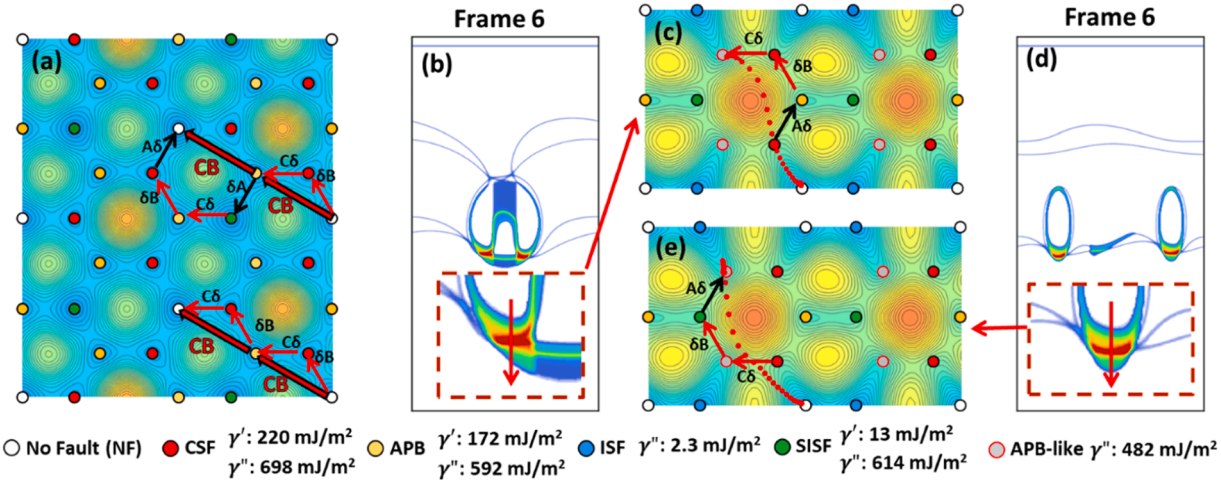

Fig. 10. (a) Deformation pathways of the γ′ phase when a coprecipitate (upper) and a monolithic precipitate (lower) interacts with CB+CB dislocation group. The shearing pathways are directly taken from Fig. 6 and Fig. S6. (b) Frame 6 of coprecipitate shearing by CB+CB+CB dislocation group and (c) the associated deformation pathways of the γ″ phase. (d) Frame 6 of monolithic precipitates shearing by CB+CB+CB dislocation group and (e) the associated deformation pathways of the γ″ phase. The red dots on (c) and (e) corresponds to the deformation pathway along the solid red arrow in the insets of (b) and (d).

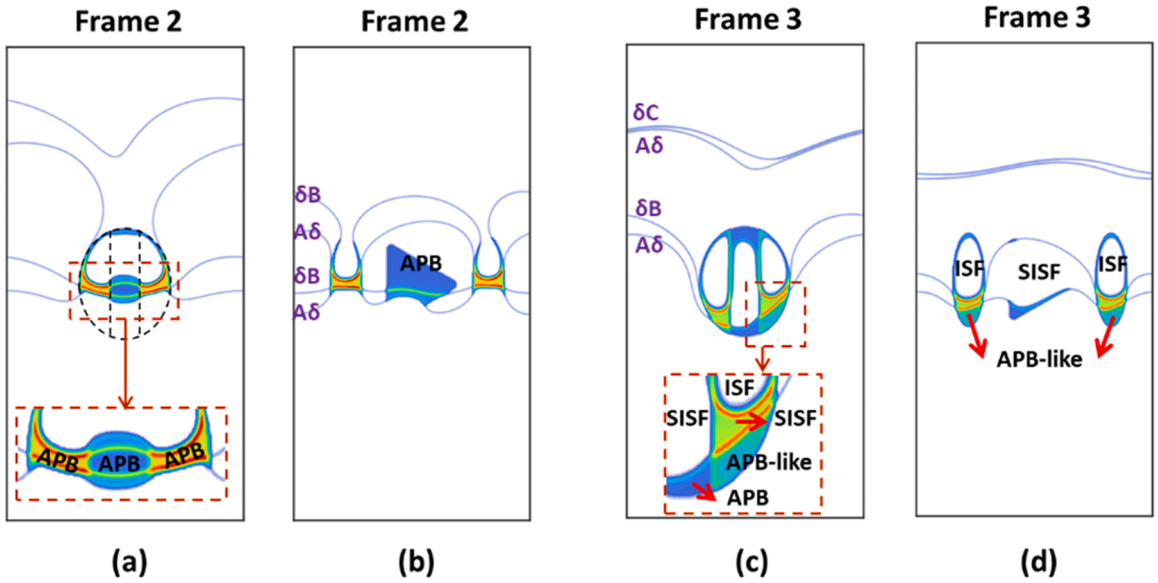

Fig. 11. Frame 2 of AB+AB dislocation shearing (a) coprecipitate and (b) monolithic precipitates. Frame 3 of AC+AB dislocation group shearing (c) coprecipitate and (d) monolithic precipitates. Fig. 11 (a), (b), (c) and (d) are directly taken from Fig. 2(a), Fig. S2(a), Fig. 4(a) and Fig. S4(a) for comparison.

due to the longer separating distance between the two γ″ particles and curved γ|γ″ interfaces. Therefore, the remnant Shockley partial does not enter the γ′ phase and creates an SISF. A side note regarding the formation of CSF in the γ′ phase is that CSF can react with APB on adjacent layer and form SISF through reordering. However, the coprecipitate may constrain such activity since the reordering process may not be favored in γ″. How the reordering mechanisms in γ′ would play out in a coprecipitate where γ′ is surrounded by γ″ is still unclear and worth exploring.

Another interesting feature is that even though the remnant Shockley partial cannot enter γ′ in monolithic precipitates, the loop still enters the matrix, but only a little along the short axis of the γ″ precipitates. Under a given applied stress, a dislocation loop will shrink and eventually disappear if it is smaller than a critical size, while expand if it is larger than the critical size. The remnant Shockley partial dislocation loop in the case of the coprecipitate is expanding in all direction into the matrix, suggesting that it is larger than the critical size and will continue expanding. In contrast, the loop in the monolithic particles is only entering the matrix along the short axis rather than in all directions, suggesting that the loop is smaller than the critical size and tends to shrink but is pinned by the γ|γ″ interface along the long axis. To minimize its energy, the loop expands near-horizontally to have more screw component that has a lower line energy as compared to that of the edge component. The difference in the motion of the remnant Shockley partial in a coprecipitate and monolithic precipitates is a result of the precipitate dimensions. In this sense, the coprecipitate acts like a big γ″ particle, the size and aspect ratio of which cannot be achieved in its monolithic form.

4.3. *Effect of misfit stress*

The current simulation does not consider the effect of misfit stress between any two of the three phases as they would not alter the deformation pathways we demonstrated above. However, the misfit stress would certainly impact on the critical stresses required to activate each

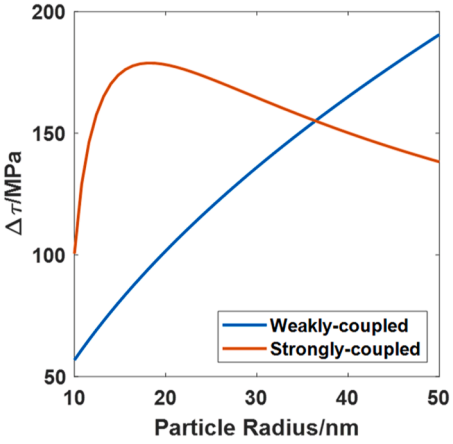

Fig. 12. Critical resolved shear stress of APB shearing with weakly- and strongly-coupled dislocations. The parameters used are as follows [35,36]. $E_{APB} = 260\ mJ/m^2$, $b = 0.253\ nm$, $f = 10\%$, $\Gamma = \alpha G b^2$, $\alpha = 0.5$, $G = 95 GPa$, $w = 1$, $A = 0.72$.

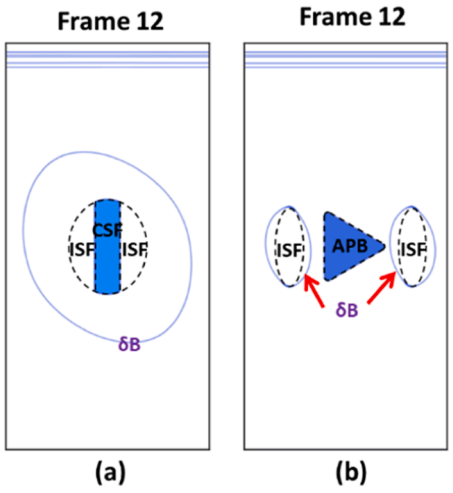

Fig. 13. Frame 12 of CB+CB+CB dislocation group shearing (a) coprecipitate and (b) monolithic precipitates. Fig. 13(a) and (b) are directly taken from Fig. 8 and S8 for comparison.

of the deformation pathways. From the evolution equation, the variational derivative of the applied stress term is $\frac{\delta(-\sigma_{ij}^{ex}\int\sum_p \varepsilon_{ij}^p \eta_p dV)}{\delta\eta_p} = -\sum_p \sigma_{ij}^{ex}\varepsilon_{ij}^p$. If we consider the misfit stress field of the coprecipitate as an external stress just like an applied stress that drives the motion of a dislocation, we can define the interaction energy between a dislocation and the misfit stress field of the coprecipitate as $I = -\sum_p \sigma_{ij}(\mathbf{r})\varepsilon_{ij}^p$, where $\sigma_{ij}(\mathbf{r})$ is the stress field of the coprecipitate and ε_{ij}^p is the eigenstrain of a dislocation [21]. A multi-phase field model has been applied to study the growth kinetics of different coprecipitate configurations [16], from which the equilibrium order parameter profiles of a dual-lobed coprecipitate are obtained (Fig. 14). Lattice parameters of the γ, γ′ and γ″ phases and the elastic constants of the γ phase are also taken from Ref [16]. The coherency stress field of the coprecipitate is then calculated, as well as the one with only the center γ′ phase, the one with a single lobe of the γ″ phase, and the one with both lobes of the γ″ phases but without the middle γ′. The interaction energy on (111) plane between these precipitates and all six $a/2\langle 110\rangle_\gamma$ dislocations are shown in Fig. 15. Note that there are three variants of the γ″ phase and the γ″ in Fig. 15 is the (001) variant where the γ″ phase grows on the (001) plane of the γ′

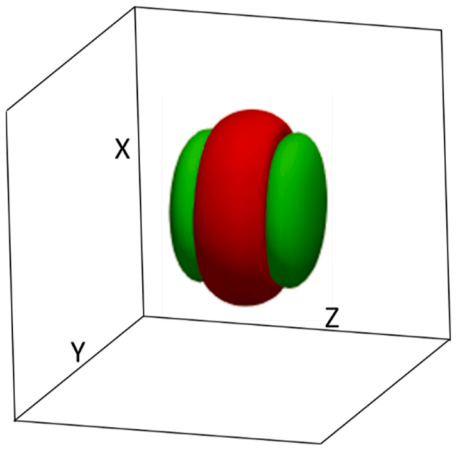

Fig. 14. Dual-lobed coprecipitates from multi-phase field simulations.

phase, and the intersection of the γ′|γ″ interface plane with the (111) slip plane is parallel to AB. Due to the 3-fold symmetry of the (111) plane as well as the equivalency of the three γ″ variants, the interaction energy between the other two variants and all six $a/2\langle 110\rangle_\gamma$ dislocations can be obtained by symmetry operations. For dislocations whose Burgers vectors are along the opposite directions with each other (like AB and BA), the interaction energy contours with the same coprecipitate have opposite signs but the same magnitude.

For the single lobe of the γ″ phase (Fig. 15(a)), an alternating positive and negative interaction energy surrounds the lobe with the maximal values at the γ|γ″ interface. Inside the precipitate, the interaction energy can be positive or negative depending on the Burgers vector of the dislocation. Adding the second lobe (Fig. 15(b)) to form the dual-lobed configuration without the γ′ greatly enhances the interaction energy for BC/CB as well as CA/AC dislocations in the γ channel between the γ″ lobes, while it reduces the interaction energy between the γ″ phase and AB or BA in the γ channel between the γ″ lobes. Adding the second lobe also decreases the magnitude of the interaction energy within the γ″ precipitate (the left γ″ lobes in the middle subfigure of Fig. 15(a) and (b)). Adding the γ′ phase (Fig. 15(c)) on top of the two lobes of the γ″ phase greatly reduces the magnitude of the interaction energy in the γ channel between the γ″ lobes because the stress field is greatly reduced for the coprecipitate as the reduction in coherency elastic energy is one of the driving forces to form coprecipitate in the first place. Moreover, the addition of γ′ in the γ channel between the two γ″ lobes further reduces the magnitude of the interaction energy within the γ″ precipitate (the left γ″ lobes in the middle subfigure of Fig. 15(b) and (c)).

Overall, from Fig. 15(a) and (c), the coprecipitate configuration reduces the effect of the misfit stress of the γ″ phase imposed on dislocations, as compared to the monolithic counterparts. In addition, for the γ′ phase, the coprecipitate configuration reverses the interaction between the γ′ precipitate and dislocations (Fig. 15(b) and (d)) because the γ′ particle in the coprecipitate is strongly coupled with the γ″ particles. The strong negative/positive interaction in the γ′ channel in between the two γ″ lobes will override the original positive/negative interaction between γ and dislocations.

4.4. *Effect of loading condition and particle size*

The current simulations assume the applied stress is along the total Burgers vector of the dislocation groups. Previous phase field simulations [27,37] have revealed that a change of the applied stress direction can drive the expansion of the remnant Shockley partial into the matrix. The expanding Shockley partial loops of the same Burgers vector on parallel slip planes may be one of the reasons why microtwins in IN718 can extend and propagate through the microstructure for several microns (see more discussions in the next section). The stress direction can

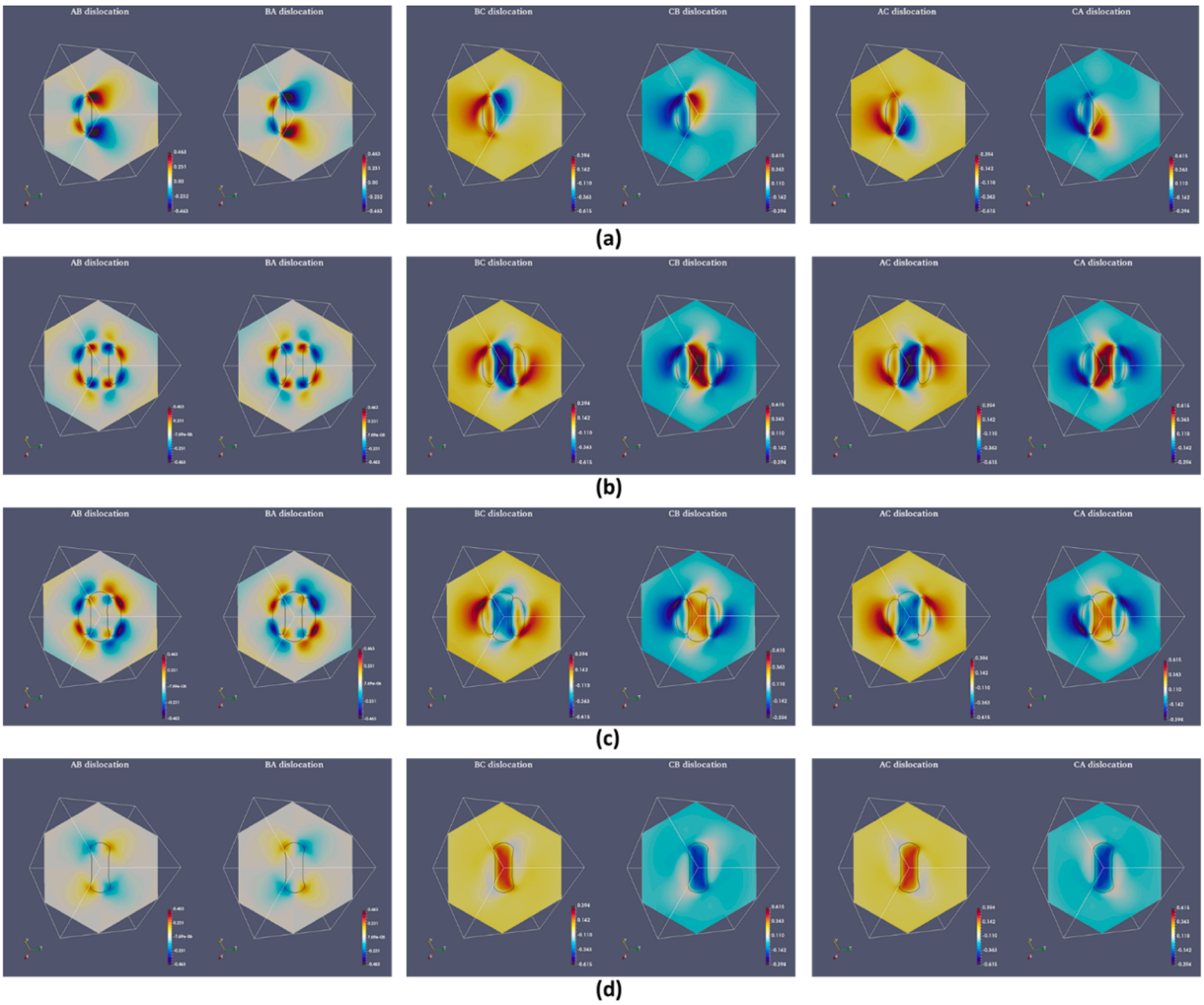

Fig. 15. Interaction energy between $a/2\langle 110\rangle_{\gamma}$ dislocations with (a) the single left lobe of the γ″ phase, (b) both lobes of the γ″ phase, (c) the dual-lobed coprecipitate and (d) the middle particle of the $\gamma^{'}$ phase.

also favor certain shearing pathways in addition to the coupling between the two phases that has already diversified the possible shearing pathways for either phase (as discussed above). The magnitude of the applied stress also matters. A high stress will activate simultaneously multiple deformation pathways, which will in turn interact with each other, while a small stress will selectively activate pathways with the lowest energy barriers. The precipitate size will also affect the shearing mechanisms. A small precipitate size can be equivalent to a large applied stress whereas a large precipitate can be equivalent to a small applied stress because of the curvature effect. In addition to precipitate shearing, there is clearly a looping vs. shearing competition as a function of both applied stress (magnitude and direction) and particle size. A deformation map is thus needed to locate specific deformation mechanisms for a given loading condition and microstructure. Such an effort has been made for γ′-strengthened Ni-based superalloys with both analytical calculations and phase field simulations where only APB shearing is considered [38]. For a system with much more complicated shearing mechanisms, it is difficult to form a set of analytical equations, but high-through-put phase field simulations can be useful in generating such a deformation map for IN718, which is worth pursuing in the future. Meanwhile, the quantitative impact from the coprecipitate on the critical resolved shear stress (CRSS) depends not only on the shearing pathways determined by the interplay between γ′ and γ″ discussed in Section 4.2 (a higher energy pathway usually leads to a larger CRSS value), but also on the coprecipitate size and inter-particle spacing. Compared to the monolithic counterparts, the coprecipitates may be stronger, but they may have larger inter-particle spacing. A more "realistic" microstructure needs to be employed to clearly elucidate the relationship between precipitate morphology (monolithic vs coprecipitate) and critical resolved shear stress.

4.5. *Stacking fault shearing vs. microtwinning*

Besides stacking fault shearing, microtwinning is another prominent deformation mechanism commonly observed in γ″-strengthened superalloys like IN718. Generally, microtwinning in IN718 is a deformation mode that has been observed primarily at higher temperatures in comparison with stacking fault shearing [39], but microtwinning was also observed at low temperature when the degree of deformation is large [26]. Besides the temperature dependence of the deformation mechanisms, what remains in question is whether there is a link between the stacking fault shearing presented above and microtwin formation. A recent simulation work discovered a dislocation transformation mechanism via GSF mismatch between a low symmetry precipitate phase (γ″) and a high symmetry matrix phase (γ), which may provide some insights into this aspect [34]. The dislocation transformation is mediated by the nucleation of a remnant Shockley partial, just like the one shown in Fig. 1(c), except that the applied stress is not perpendicular to the Burgers vector of the remnant Shockley partial and, thus, will drive the partial to expand into the matrix. If an array of the full dislocation shear

through the precipitates like Fig. 4(c), an array of remnant Shockley partials would be generated, i.e., a Shockley partial source [34]. The ISFs left behind in the γ″ phase serve as precursors to extrinsic stacking fault (ESF) (e.g., if the ISFs on two adjacent layers overlap with each other), which is a precursor to twins (ISFs on multiple adjacent layers overlap with each other).

One can imagine the following scenario. There are three γ″ variants in the microstructure, all of which can be sheared on multiple consecutive slip planes (see the schematic drawings in Fig. 16). Let's denote the variant we have studied above as variant 2 (v2) in Fig. 16, and the other two as variant 1 (v1) and variant 3 (v3). Two (111) planes (labeled slip plane 1 and slip plane 2) are shown in the figure. Consider a full dislocation (CB) gliding on slip plane 1 (Step 1, Fig. 16(a), slip plane 1). Following the shearing mechanisms (deformation pathways) in Fig. 17, the CB dislocation would create an ISF in v1 and v2, with Cδ partial looping v1, remnant partial δA looping v2, and δB+Cδ looping v3 (Step 2, Fig. 16(b), slip plane 1). The remnant partial δA can then expand into the γ matrix under the applied stress, looping v1 and shearing v3. The final stacking fault configuration after CB shearing is ISF in all three variants, with δA+Cδ looping v1, δB+Cδ looping v3, and remnant Shockley partial δA expanding in all directions (Step 3, Fig. 16(c), slip plane 1). Then the full dislocation may climb or double cross-slip onto the adjacent slip plane 2 (Step 3, Fig. 16(c)), and it will shear another set of γ″ variants that are in its way on slip plane 2, creating ISF in v1 and v2, with Cδ partial looping v1, remnant partial δA looping v2 and δB+Cδ looping v3 (Step 4, Fig. 16(d), slip plane 2). The remnant Shockley partial δA on slip plane 2 will be expanding in all directions (Step 5, Fig. 16(e), slip plane 2), just like the scenario on slip plane 1. Once it encounters the precipitates that have been sheared on slip plane 1, it will shear v3 while loops v1 and v2 (Step 6, Fig. 16(f), slip plane 2). Similarly, the remnant Shockley partial δa on slip plane 1 will continue to expand and interact with the precipitates that have been sheared by CB on slip plane 2, creating ISF in v3 while looping v1 and v2 (Step 6, Fig. 16(f), slip plane 1). Since two ISF on two adjacent (111) planes is an ESF, which is the precursor for twin formation, one could imagine the formation of a twin in v3 through the mechanism above if the CB can continuously climb or cross-slip on multiple adjacent (111) planes or other CB dislocations are operating on adjacent (111) planes.

In addition, for a stream of CB ($a/2\langle 110\rangle_\gamma$) dislocations gliding on one slip plane, the dislocation transformation mechanism will transformation them into $a/2\langle 112\rangle_\gamma$ dislocations (CB+CA) [34]. This means that, even with a single full dislocation source (CB), there will be two types of full dislocations on the source plane (CB and CA), both of which can climb and cross slip onto adjacent slip planes and create remnant Shockley partial that can expand in the matrix and shear other variants of γ″ phases, leading to the formation of ISF and twins within γ″ (CB for v3 and CA for v1, see deformation pathway in Fig. 17). This analysis may shed some light on the link between the stacking fault shearing process and microtwin formation. Since this process depends on climb or cross-slip, it may also contribute to the temperature dependence of the deformation modes in this alloy. However, the actual operating mechanisms could be much more complicated and are certainly beyond the scope of the current study.

5. Summary

We use an *ab-initio*-informed microscopic phase field model to study systematically the shearing mechanisms of a dual-lobed γ″|γ′|γ″ coprecipitate in a Ni-based superalloy, IN718. A variety of stacking fault configurations created by different dislocation groups are identified and documented, in particular $ISF_{\gamma''}|SISF_{\gamma'}|ISF_{\gamma''}$ and $ISF_{\gamma''}|APB_{\gamma'}|ISF_{\gamma''}$ (and its variant $ISF''_{\gamma}|CSF_{\gamma'}|ISF_{\gamma''}$) that can be observed experimentally. We also conducted parallel phase field simulations with monolithic γ′ and γ″ precipitates and probed the coupling effects between the two phases in the dual-lobed coprecipitate on the shearing processes. The coupling effects include the following three aspects: First, dislocations are forced to go through high energy pathways in both phases in the coprecipitate that would not be visited by the dislocations if they were in their monolithic forms. Second, for the same pathway, the stacking fault

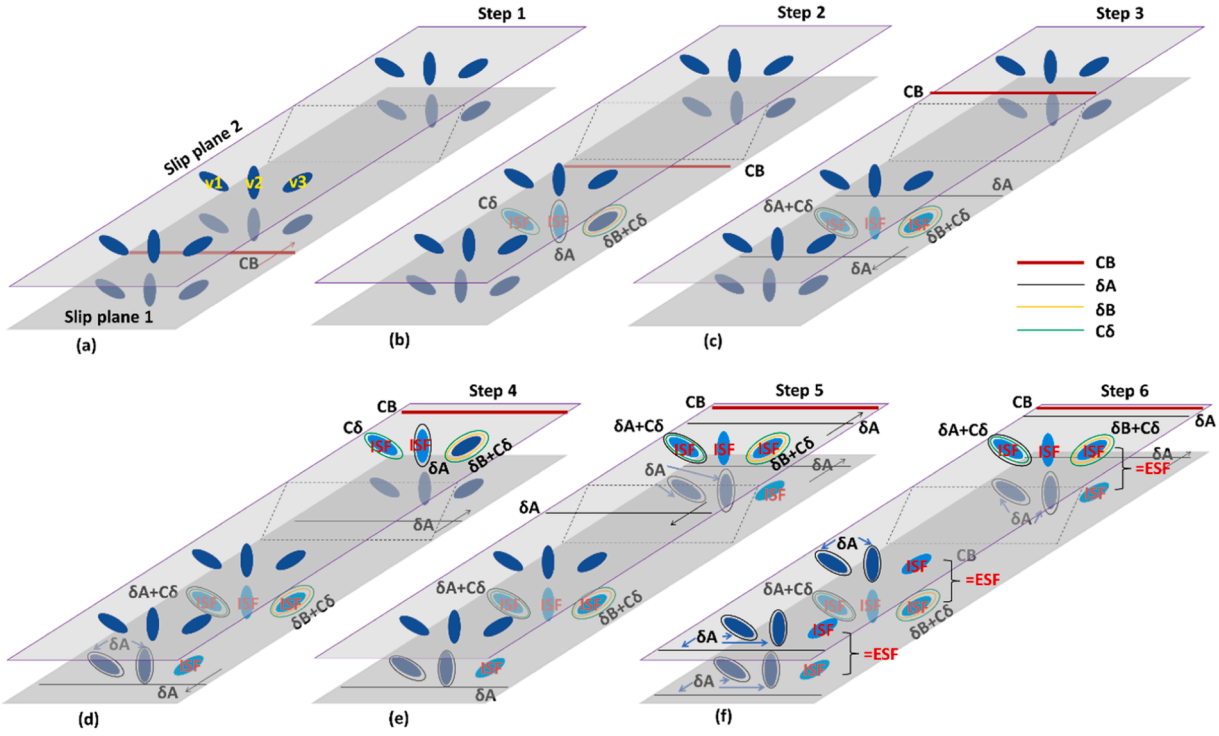

Fig. 16. Schematic illustration of ESF formation in one variant of the γ″ precipitates (v3) through cross-slip of a single $a/2\langle 110\rangle_\gamma$ dislocation (CB). From (a) to (f), the one full dislocation CB glides on slip plane 1 and then cross slip to slip plane 2. During this process, it shears variant 1 and 2 directly and creates Shockley partial δA on both planes. The δA partial then shears variant 3 on both planes and create ESF.

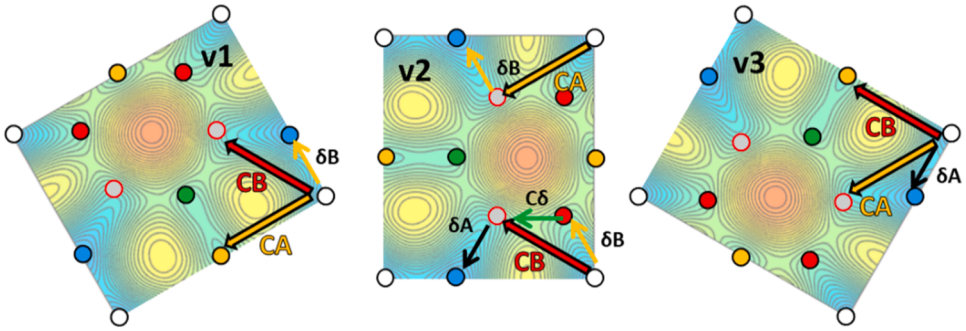

Fig. 17. Deformation pathways of CB, CA and their corresponding remnant Shockley partial dislocations δB, δA, with three variants of the γ″ phase.

configuration in the coprecipitates can be different from that in the monolithic ones. Higher stress is needed to create some of the stacking fault configurations in the coprecipitates. Both effects would increase the alloy strength. Third, the geometry of the dual-lobed coprecipitate, i.e., parallel and flat γ′|γ″ interface, could lead to new stacking fault configurations due to the strong elastic interaction between partial dislocation loops surrounding the γ″ precipitates. The results from this work clearly demonstrate the complicated shearing processes of a coprecipitate that would otherwise be absent for monolithic precipitates, which offers new opportunities for alloy design by taking advantages of possible synergistic effects on alloy strength from coprecipitates microstructures. However, more work is needed to develop a comprehensive deformation mechanism map that considers all loading conditions and coprecipitate configurations (including compact and single-lobed coprecipitates).

Declaration of Competing Interest

The authors declare that they have no known competing financial interests or personal relationships that could have appeared to influence the work reported in this paper.

Acknowledgements

The authors would like to acknowledge the financial support from NSF DMREF program under grant DMR-1922239. CHZ acknowledges sponsorship provided by the Alexander von Humboldt foundation through a Feodor-Lynen Research Fellowship. This work was performed (LF) in part under the auspices of the U.S. Department of Energy by Lawrence Livermore National Laboratory under Contract No. DE-AC52-07NA27344.

Supplementary materials

Supplementary material associated with this article can be found, in the online version, at doi:10.1016/j.actamat.2023.118693.

References

[1] M.J. Donachie, S.J. Donachie, Superalloys: A Technical Guide, ASM international, 2002.
[2] R. Cozar, A. Pineau, Morphology of γ'and γ" precipitates and thermal stability of inconel 718 type alloys, Metall. Trans. 4 (1973) 47–59.
[3] A.J. Detor, R. DiDomizio, R. Sharghi-Moshtaghin, N. Zhou, R. Shi, Y. Wang, D. P. McAllister, M.J. Mills, Enabling large superalloy parts using compact coprecipitation of γ′ and γ″, Metall. Mater. Trans. A 49 (2018) 708–717.
[4] S. Mukhopadhyay, H. Sriram, C.H. Zenk, R. DiDomizio, A.J. Detor, R.W. Hayes, G. B. Viswanathan, Y. Wang, M.J. Mills, Creep behavior of compact γ′-γ ″coprecipitation strengthened IN718-variant superalloy, Metals 11 (2021) 1897.
[5] T. Alam, M. Chaturvedi, S.P. Ringer, J.M. Cairney, Precipitation and clustering in the early stages of ageing in Inconel 718, Mater. Sci. Eng. 527 (2010) 7770–7774.
[6] D. McAllister, D. Lv, B. Peterson, H. Deutchman, Y. Wang, M.J. Mills, Lower temperature deformation mechanisms in a γ ″-strengthened Ni-base superalloy, Scr. Mater. 115 (2016) 108–112.
[7] J. He, G. Han, S. Fukuyama, K. Yokogawa, Interfaces in a modified Inconel 718 with compact precipitates, Acta Mater. 46 (1998) 215–223.
[8] G.A. Rao, M. Kumar, M. Srinivas, D.S. Sarma, Effect of standard heat treatment on the microstructure and mechanical properties of hot isostatically pressed superalloy inconel 718, Mater. Sci. Eng. 355 (2003) 114–125.
[9] E. Chlebus, K. Gruber, B. Kuźnicka, J. Kurzac, T. Kurzynowski, Effect of heat treatment on the microstructure and mechanical properties of Inconel 718 processed by selective laser melting, Mater. Sci. Eng. 639 (2015) 647–655.
[10] M.M. Kirka, K.A. Unocic, N. Raghavan, F. Medina, R.R. Dehoff, S.S. Babu, Microstructure development in electron beam-melted Inconel 718 and associated tensile properties, JOM 68 (2016) 1012–1020.
[11] W. Ma, Y. Xie, C. Chen, H. Fukanuma, J. Wang, Z. Ren, R. Huang, Microstructural and mechanical properties of high-performance Inconel 718 alloy by cold spraying, J. Alloys Compd. 792 (2019) 456–467.
[12] T. Trosch, J. Strößner, R. Völkl, U. Glatzel, Microstructure and mechanical properties of selective laser melted Inconel 718 compared to forging and casting, Mater. Lett. 164 (2016) 428–431.
[13] D. Jinhui, L. Xudong, D. Qun, L. Ying, Effect of solution treatment on the microstructure and mechanical properties of IN718 alloy, Rare Met. Mater. Eng. 46 (2017) 2359–2365.
[14] F. Theska, A. Stanojevic, B. Oberwinkler, S.P. Ringer, S. Primig, On conventional versus direct ageing of Alloy 718, Acta Mater. 156 (2018) 116–124.
[15] Sriram, H.; Kadivel, K.; Mukopadhyay, S.; Mills, M. J.; Wang, Y., Formation mechanisms of coprecipitates in incobel 718 superalloys, Acta Mater., Submitted. (n.d.).
[16] R. Shi, D.P. McAllister, N. Zhou, A.J. Detor, R. DiDomizio, M.J. Mills, Y. Wang, Growth behavior of γ'/γ″ coprecipitates in Ni-Base superalloys, Acta Materialia. 164 (2019) 220–236.
[17] T.M. Smith, R.R. Unocic, H. Deutchman, M.J. Mills, Creep deformation mechanism mapping in nickel base disk superalloys, Mater. High Temp. 33 (2016) 372–383.
[18] L. Kovarik, R.R. Unocic, J. Li, P. Sarosi, C. Shen, Y. Wang, M.J. Mills, Microtwinning and other shearing mechanisms at intermediate temperatures in Ni-based superalloys, Prog. Mater Sci. 54 (2009) 839–873.
[19] R.R. Unocic, G.B. Viswanathan, P.M. Sarosi, S. Karthikeyan, J. Li, M.J. Mills, Mechanisms of creep deformation in polycrystalline Ni-base disk superalloys, Mater. Sci. Eng. 483 (2008) 25–32.
[20] J.M. Oblak, D.F. Paulonis, D.S. Duvall, Coherency strengthening in Ni base alloys hardened by DO 22 γ′ precipitates, Metall. Trans. 5 (1974) 143.
[21] N. Zhou, C. Shen, M.J. Mills, J. Li, Y. Wang, Modeling displacive–diffusional coupled dislocation shearing of γ′ precipitates in Ni-base superalloys, Acta Mater. 59 (2011) 3484–3497.
[22] V.A. Vorontsov, C. Shen, Y. Wang, D. Dye, C.M.F. Rae, Shearing of γ′ precipitates by a< 1 1 2>dislocation ribbons in Ni-base superalloys: A phase field approach, Acta Mater. 58 (2010) 4110–4119.
[23] L. Feng, D. Lv, R.K. Rhein, J.G. Goiri, M.S. Titus, A. Van der Ven, T.M. Pollock, Y. Wang, Shearing of γ' particles in Co-base and Co-Ni-base superalloys, Acta Mater. 161 (2018) 99–109.
[24] D.C. Lv, D. McAllister, M.J. Mills, Y. Wang, Deformation mechanisms of D022 ordered intermetallic phase in superalloys, Acta Mater. 118 (2016) 350–361.
[25] A.R. Khoei, G.T. Eshlaghi, S. Shahoveisi, Atomistic simulation of creep deformation mechanisms in nickel-based single crystal superalloys, Mater. Sci. Eng. 809 (2021), 140977.
[26] M. Sundararaman, P. Mukhopadhyay, S. Banerjee, Deformation behaviour of γ ″strengthened Inconel 718, Acta Metall. 36 (1988) 847–864.
[27] C.H. Zenk, L. Feng, D. McAllister, Y. Wang, M.J. Mills, Shearing mechanisms of co-precipitates in IN718, Acta Mater. 220 (2021), 117305.
[28] C. Shen, Y. Wang, Phase field model of dislocation networks, Acta Mater. 51 (2003) 2595–2610.
[29] Y.U. Wang, Y.M. Jin, A.M. Cuitino, A.G. Khachaturyan, Nanoscale phase field microelasticity theory of dislocations: model and 3D simulations, Acta Mater. 49 (2001) 1847–1857.
[30] Y. Wang, J. Li, Phase field modeling of defects and deformation, Acta Mater. 58 (2010) 1212–1235.
[31] A.G. Khachaturyan, Theory of Structural Transformations in Solids, Courier Corporation, 2013.
[32] S.M. Allen, J.W. Cahn, A microscopic theory for antiphase boundary motion and its application to antiphase domain coarsening, Acta Metall. 27 (1979) 1085–1095.

[33] D. Hull, D.J. Bacon, Introduction to Dislocations, Butterworth-Heinemann, 2001.
[34] L. Feng, M.J. Mills, Y. Wang, Generalized stacking fault energy surface mismatch and dislocation transformation, npj Comput. Mater. 7 (2021) 1–8.
[35] S.I. Rao, T.A. Parthasarathy, D.M. Dimiduk, P.M. Hazzledine, Discrete dislocation simulations of precipitation hardening in superalloys, Philos. Mag. 84 (2004) 3195–3215.
[36] E. Nembach, G. Neite, Precipitation hardening of superalloys by ordered γ′-particles, Prog. Mater Sci. 29 (1985) 177–319.
[37] L. Feng, D. McAllister, C.H. Zenk, M.J. Mills, Y. Wang, Deformation mechanisms of γ′ and γ ″Co-precipitates in IN718. Superalloys 2020, Springer, 2020, pp. 669–679.
[38] R.R. Unocic, N. Zhou, L. Kovarik, C. Shen, Y. Wang, M.J. Mills, Dislocation decorrelation and relationship to deformation microtwins during creep of a γ′ precipitate strengthened Ni-based superalloy, Acta Mater. 59 (2011) 7325–7339.
[39] D.P. McAllister, Shearing Mechanisms and Complex Particle Growth in Nickel Superalloy 718, The Ohio State University, 2016.